

# **Manufacturing and tribological behavior of self-lubricating duplex composites: graphite-reinforced polymer composites and polymer-infiltrated-metal-networks**

Yinyin Zhang<sup>1^</sup>, David Chern<sup>1</sup>, Robert Schulz<sup>2</sup>, Janine Mauzeroll<sup>3</sup>, Richard R. Chromik<sup>1\*</sup>

<sup>1</sup>Department of Materials Engineering, McGill University, 3610 University Street, Montreal, QC, H3A 0C5, Canada

<sup>2</sup>Hydro-Québec Research Institute (IREQ), Varennes, QC, J3X 1S1, Canada

<sup>3</sup>Department of Chemistry, McGill University, 3420 University Street, Montreal, QC, H3A 2A7, Canada

<sup>^</sup>Current address: Ecole des Mines de Saint-Etienne, SMS Division, 42023 Saint-Etienne, France

\*Corresponding author: richard.chromik@mcgill.ca (Richard R. Chromik)

## **Abstract**

Self-lubricating duplex composites comprising a top layer of polymer-based composites, i.e. bismaleimide (BMI) filled with a wide range of graphite (Gr) content (0-55 wt%), and a bottom layer of infiltrated metal-networks were manufactured by a hot compression-molded method. Melting points and polymerization temperatures of as-received BMI powder and BMI+Gr blends were investigated to determine infiltration process. The polymerization peaks are pushed to higher temperatures with graphite content. For cured polymer composites, the hardness measured by nanoindentation keeps increasing with the graphite content up to 55% without degradation. Tribological performance of the top and bottom composites are examined individually, with focus placed on the development and stability of lubricating transfer film and tribofilm. For the top polymer composites, 25 wt%Gr (or equivalently 17 vol%) is sufficient to form lubricating transfer film and reduces the friction to the lowest ~0.15. For the bottom infiltrated metal-networks, the BMI+55%Gr-infiltrated network is adequate to develop fully covered transfer films and achieve low friction throughout the test. Those results shed lights on design and manufacturing of self-lubricating polymer matrix composites on metallic components that undergo severe running conditions.

**Key words:** polymer-based composites; self-lubricating duplex composites; friction; transfer film

# 1 Introduction

Rapidly growing concerns for environmental sustainability and energy consumption have driven demands for longer lifetime and higher efficiency of transportation and industrial infrastructure [1, 2]. A recent study by Holmberg *et al.* [2] demonstrated that a substantial amount of energy, i.e. ~20% of total energy globally, is lost due to friction and wear; 18-40% of the energy loss can be eliminated by advanced developments in tribology such as lubricants, new materials and designs. Among those advanced design strategies are self-lubricating composites, which are an important class of materials that incorporate solid lubricants into a matrix to provide continuous replenishment of lubricant throughout service [3, 4]. This design often meets requirements when materials are subjected to extreme conditions, such as high contact stress, elevated temperature and corrosive environment where fluid lubricants cannot be adapted [5-9]. Self-lubricating metal matrix composites incorporated with solid lubricants have been manufactured using various techniques such as casting, powder metallurgy, laser cladding, friction stir, thermal spray and cold spray; their tribological performance have been well investigated and recently reviewed by Zhang *et al.* [6] and Torres *et al.* [9]. Compared to metal matrix composites, self-lubricating polymer-based composites that own well-known advantages such as lighter weight, cheaper processing and easier maintenance, are less understood, in particularly, in terms of their tribological behaviour [10, 11].

Bismaleimides (BMI) are thermally stable thermosetting polyimides and an important member of high-performance matrix resins due to their better thermal stability and mechanical properties than epoxy resins, as well as easier processing than polyimides [12, 13]. BMI-based composites incorporating solid lubricants have been used for tribological applications in aerospace where high contact stress and/or elevated temperature may take place. Tewari *et al.* [14] reported in 1988 that BMI composites containing MoS<sub>2</sub> or PTFE yielded improved friction and wear characteristics, particularly at high loads. With recently emerging nanofillers for polymer composites, BMI and other polymers have been widely utilized to load more advanced nanofibers such as carbon nanotubes (CNTs), graphene, and nanometer-sized solid lubricants and oxides [7, 8, 15-17]. Those nanocomposites often exhibit enhanced mechanical and tribological properties [7, 8]. For example, Yan *et al.* [18] fabricated BMI + reduced graphene oxide (rGO) composites and their results demonstrated that 0.6 wt% addition of rGO gave the highest impact and flexural strength, and

reduced friction by 45% and wear rate by 77% compared to those of pure BMI. However, a challenge in processing self-lubricating nanocomposites resides in the agglomeration of nanofillers, which often causes degradation of mechanical properties and tribological performance. Hence, the highest achievable nanofiller content was limited to around 3 wt% or below [7, 8, 18, 19].

In the present study, to avoid agglomeration and achieve a high concentration of solid lubricant (i.e. up to 50 wt%), a submicron-sized graphite was chosen; a BMI that is advertised as high strength, good loading capacity of fillers, was selected as matrix material. A novel duplex composite structure was designed. That is, BMI-based composites were infiltrated into porous metallic network, leading to duplex layers consisting of a topmost polymeric composite and a subsurface layer of polymer-infiltrated metal network. Another important reason why submicron-sized graphite was selected was that larger graphite size, e.g. several micron meters, may prevent them from infiltration and achieving homogeneous filler distribution inside both layers of the composites. The present duplex composites introduce two significant benefits on tribological applications; one is improved bonding strength between the self-lubricating polymer and metallic part without using adhesives or glues, the other is persistent replenishment of lubricant when the topmost layer wears away. It is important to point out that the current work serves as a proof-of-concept to study what characteristics of such a structure are important in determining properties and performance. Future engineering applications are directed to surface protection of two types of components; first are metallic foams or 3-D printed structures that could be impregnated with polymers, second are porous coatings made by thermal spray or others. For example, using acid leaching, Nascimento *et al.* [20] tailored porosity of a stainless steel coating made by high-velocity oxygen fuel spray for further step of polymer infiltration. Here, using pre-fabricated, commercially available porous metal networks, we investigate infiltration process, thermal and mechanical properties of the BMI+Gr composites, as well as tribological behaviour of each composite layer, with focus placed on development and stability of lubricating transfer film and tribofilm at the contact.

## **2 Materials and experimental**

### **2.1 Polymer testing and processing window**

A commercial Bismaleimide VTEC PI-1031 (VTEC, USA) with an average particle size of  $\sim 19$   $\mu\text{m}$  in diameter was used in the present study. To determine the infiltration and curing process, thermal properties of the as-received BMI were investigated. Using a Thermogravimetric analyzer (TGA Q500, TA instruments), samples were heated up to  $680^\circ\text{C}$  at a rate of  $10^\circ\text{C}/\text{min}$ . The same heating rate was employed for differential scanning calorimetry (DSC Q2000, TA instruments), where temperature raised to  $250^\circ\text{C}$  from  $25^\circ\text{C}$ . Fig. 1a shows TGA results, where thermal degradation of the as-received powder is a two-step process. The first significant mass reduction, i.e. 41% of the total mass, takes place at around  $400\text{--}548^\circ\text{C}$ . This indicates the BMI is thermally stable up to  $\sim 400^\circ\text{C}$  with only a minor mass loss of 2% which is likely due to evaporation of moisture and other adsorbed contaminants. The second major thermal degradation of the BMI occurs at  $\sim 600^\circ\text{C}$ , which was probably attributed to carbonization of the hydro-carbonated compounds [21]. From DSC result shown in Fig. 1b, the endothermic reaction starting at  $\sim 72^\circ\text{C}$  corresponds to melting process and the peak value ( $T_m$ ) is at  $78^\circ\text{C}$ . With increasing temperature, an exothermic reaction occurred at  $150^\circ\text{C}$  ( $T_i$ ), resulting from cross-linking of the cure process, followed by the polymerization peak ( $T_p$ ) at  $197^\circ\text{C}$ , which is the temperature where the highest polymerization rate was achieved. The low melting point and high polymerization temperature led to a wide processing window of the selected BMI.

Wettability of a liquid over a solid surface serves as a good measure of the adhesion force between the two interfaces, which has been applied in some industries like oil, liquid coating, printing, and it is best measured via contact angles that vary with temperature [22-25]. In the present study, contact angles of the BMI on a polished stainless steel over melting were measured and it showed the lowest of  $\sim 45^\circ$  at  $138^\circ\text{C}$  (see inset of Fig. 1b), indicating fairly easy spreading and strong bonding of the liquid BMI onto the stainless steel [22] [24]. In addition, the wettability measurement demonstrates the flowability of the BMI during melting most likely reaches the lowest at  $\sim 138^\circ\text{C}$ .

To cover a wide range of filler content and produce composites with high fractions of solid lubricant for tribological applications, three blends containing 25, 40, and 55 wt% graphite were examined here. Worth to note our preliminary tests (not shown) indicated poor integrity of composites with graphite higher than 55 wt% under the present processing condition. From Fig. 2a, addition of graphite shifts the melting point to slightly higher temperatures. BMI + 55% Gr has

a melting point of  $\sim 80^\circ\text{C}$ ,  $1^\circ\text{C}$  higher than that of BMI + 40% Gr whose melting point is  $1^\circ\text{C}$  higher than that those of BMI + 25% Gr and pure BMI. However, since the temperature deviation induced by graphite is minor, infiltration temperature was selected as  $138^\circ\text{C}$  for all composites. In Fig. 2b, the major polymerization peaks of the BMI + Gr blends are significantly pushed towards higher temperatures by  $70\text{--}90^\circ\text{C}$ , and maximum peak temperatures are  $270^\circ\text{C}$ ,  $282^\circ\text{C}$ ,  $285^\circ\text{C}$  with increase in graphite content. Meanwhile, the magnitude of the peaks reduces. Those are likely due to interaction of BMI and graphite during polymerization [25]. Given that the high graphite content ( $\geq 25\%$ ), small graphite size ( $\sim 0.5\ \mu\text{m}$ ), and high molecular weight of the BMI in the present study, a high specific interfacial area, polymer-graphite interfacial area per unit volume, is expected. Hence, noncovalent interaction between BMI and graphite fillers by bridging and wrapping are likely to occur. Then polymerization of the BMI through double bond of BMI is slowed down and decreases in numbers, which contributes to the higher polymerization temperatures and weak polymerization peaks of the BMI+Gr blends. Bridging and wrapping were observed frequently from both experiments and simulations when various polymers were interacting with unfunctionalized carbon nanotube [25]. Consequently, the optimized polymerization temperature for the BMI + Gr composites was set at  $\sim 235^\circ\text{C}$ , between **T<sub>i</sub>** and **T<sub>p</sub>**, higher than that of neat BMI ( $\sim 190^\circ\text{C}$ ).

## 2.2 Infiltration process and mechanical property testing

Three blends of BMI and graphite (Asbury,  $d_{50} = 0.5\ \mu\text{m}$ ) with different weight fractions of 25%, 40%, 55% were prepared by mechanical mixing using a planetary ball mill (PM 400, Retsch). The mixtures were then poured onto porous SS316L discs (McMaster-Carr) that are 1.5 inches ( $\sim 38\ \text{mm}$ ) in diameter, 0.0625-inch ( $\sim 1.6\ \text{mm}$ ) thick (see Fig. 3b). The pores are interconnected and take  $\sim 50\%$  volume of the disc, and the minimum pore size is roughly  $10\ \mu\text{m}$ . The infiltration was conducted by a hot compression-molded method that included two steps: infiltration and curing. As shown in Fig. 3a, the former was set at a temperature of  $\sim 138^\circ\text{C}$  while keeping the pressure constant at 2 MPa for 1 hour, and immediately after, the pressure increased to 3 MPa while temperature started rising to the polymerization temperature of  $235^\circ\text{C}$ . All specimens were cured on the hot press for 2 hours and then the system cooled down to  $\sim 60^\circ\text{C}$  in air before opening the platens. This led to a relatively lower cooling rate than opening the platens at higher temperatures. Based on our preliminary tryouts, the latter promoted formation and growth of cracks, in particular

at metal-polymer interfaces, which was attributed to discrepancy in thermal expansion coefficients of the metal and polymer [26]. Fig. 3c shows schematically the resultant duplex composite including the polymer composite and infiltrated metal network. Neat BMI was also processed under identical condition with a lower polymerization temperature of 190 °C according to its thermal properties (see Fig. 2b).

Hardness and Young's modulus of the cured BMI and BMI + Gr composites were examined by nanoindentation (Hysitron, Ubi3, USA) equipped with a Berkovich diamond tip. Indentation tests were carried out from mechanically polished cross-sectional surfaces. The duplex composites were firstly cut using a slow-speed diamond blade, then cold-mounted and mechanically ground and polished down to 1 µm oil-based diamond suspension, and finally vibratory polished using 0.05 µm colloidal silica for 24 hours to remove or minimize fine scratches induced by previous grinding and polishing. A load function of 20 s linear loading to a peak load of 5 mN and holding of 30 s and 5 s linear unloading was used for the nanoindentation. A long dwell time at the peak load employed here was to exhaust viscoelastic creep and minimize the creep rate during the unloading curve [27]. The load function here that led to indents of ~5-6 µm in size was also to cover BMI and Gr such that it revealed mechanical property of the composite. Hardness and elastic modulus values were calculated by Oliver and Pharr [28] method and the values presented here are averages of at least 30 indents (i.e. 5×6 grid) for each material.

### **2.3 Tribological tests and post-characterizations**

Reciprocating sliding wear tests were conducted on each layer of the duplex composites using a custom-built tribometer [29] at an ambient temperature of 21-24 °C and a relatively humidity of 30-50%. The friction forces were measured by a piezoelectric sensor at a sampling rate of 800 Hz. Hardened martensitic steel AISI 440C balls with a diameter of 6.35 mm were used as counterfaces and were loaded with a normal force of 10.79 N. Therefore, mean Hertzian contact pressures on the neat BMI, BMI+25%Gr, BMI+40%Gr, and BMI+55%Gr were, respectively, 115 MPa, 155 MPa, 168 MPa, and 170 MPa. The sliding speed was set at 10 mm/s and the track length was 20 mm. This gave a PV (i.e. pressure \* velocity) factor of 1.15-1.70 MPa\*m/s. Long tests of 3000 cycles were performed to observe steady-state friction and wear. To study tribological behaviour of the infiltrated metal networks, the top polymer composites were removed by grinding and the

surface were then finished by polishing down to 1  $\mu\text{m}$  diamond suspension prior to sliding wear tests. Stripe tests [30, 31] were conducted with the same down force and sliding speed to examine intermediate stages of formation of lubricating tribofilms and transfer films. They started with a track length of 20 mm and shortened to 15 mm at 1000 cycles, then shortened to 10 mm at 2000 cycles and kept running for another 2000 cycles before it further shortened to 5 mm, where an additional 4000 cycles were conducted. Three repeatable tests were performed under each condition for the top polymer composites and underneath infiltrated composites.

In order to calculate the initial mean Hertzian contact pressure, the equivalent elastic moduli of the infiltrated composites were predicted using the Kerner equation that was found to fit well with the experimental data of polymer composites reinforced with rigid fillers [32-34]:

$$\frac{E_c}{E_p} = 1 + \frac{15(1-\nu_p)}{8-10\nu_p} \frac{\phi_F}{1-\phi_F} \quad (1)$$

where  $E_c$  and  $E_p$  are elastic moduli of the composite and the polymer, respectively,  $\nu_p$  is Poisson ratio of the polymer,  $\phi_F$  volume fraction of the metal. When substituting the present data,  $\phi_F=50\%$ ,  $\nu_p=0.34$ ,  $E_c= 14, 22, 25, 26$  GPa for the composites containing 0, 25%, 40%, 55%Gr, were obtained respectively. Then the initial mean Hertzian contact pressures were ~238, 317, 349, 352 MPa with increasing graphite content. However, the Kerner equation has generally been used for composites where the rigid reinforcement does not form an interconnected network. In the present study, the metal matrix is interconnected and for that reason these estimations of elastic moduli using the Kerner equation are likely a lower limit.

After sliding wear tests, morphology of the wear tracks and counterfaces were examined by an optical microscope (MA100N, Clemex, Canada) and a non-contact optical profiler (Zygo, USA). Wear rates were calculated using normalized volumetric method, as shown in equation (2):

$$\text{wear rate} = \frac{V}{N \cdot D} \quad (2)$$

where  $V$  is wear volume ( $\text{mm}^3$ ) that equals the volume below the unworn surface subtracting the volume above the unworn surface,  $N$  applied normal load (N) and  $D$  sliding distance (m). As wear volume was only measured at the end of the test, wear rate here is an average value of the entire test and does not reveal its evolution with cycle numbers. Each data reported here are mean value and standard deviation of three repeat tests. An inVia Raman microscope (Renishaw, UK)

equipped with a laser source of  $\lambda = 785$  nm was used to examine formation of the lubricating tribofilms and transfer films.

### **3 Results and discussion**

#### **3.1 Morphology, thermal and mechanical properties of the duplex composites**

From Fig. 4, infiltration depth of the polymer measured from cross-sectional micrographs decreases with increasing graphite content. The entire porous disc, i.e.  $\sim 1600$   $\mu\text{m}$  thick, is filled with BMI when there is no graphite filler (see inset a1). The infiltration depth reduces to  $\sim 910$   $\mu\text{m}$  with 25 wt% graphite added, to  $\sim 735$   $\mu\text{m}$  with 40 wt% graphite, and to  $\sim 185$   $\mu\text{m}$  when the graphite content increases to 55 wt%. In the inset a2, infiltration front of BMI+55%Gr appears wavy, resulting in a larger standard deviation of the depth value (see Fig. 4a). The significantly decreased infiltration depth with graphite content reveals infiltration becomes more challenging when submicron-sized graphite fillers was added, which is likely due to reduced flowability of the melted composites during infiltration. Such influence of fillers was also observed in other polymer composites filled with carbon nanotubes and graphite, where melt viscosity increased significantly with increasing filler content [35, 36]. However, given the high graphite content achieved in the present study (i.e. 55 wt% or 43 vol%), the current BMI grade has demonstrated a good capacity of loading fillers. As shown in the insets of Fig. 4a, the top polymer layers are often dense and void-free, and 200-500  $\mu\text{m}$  in thickness, yet pores start appearing inside polymers of the infiltrated metal networks and area fractions are 3-5%. From Fig. 4b, there are two types of pores; some of them are round and formed inside polymers, while the others are irregular and often adjacent to metal. The former is most likely introduced by gas that is trapped in the polymer during infiltration, which leads to nucleation of round voids upon polymerization. For the irregular voids, even though original pores in the metal network are interconnected, some small ones that are far from the polymer flow could remain unfilled due to lack of pressure and/or flowability. Giving that 3 MPa normal pressure is approaching the limit of the hot press and it is indeed much higher than those of BMI-based composites processed by same technique found in literature [37, 38], those pores may not be eliminated by increasing pressure only.



The glass transition temperatures ( $T_g$ ) of the cured BMI and BMI+Gr composites were measured by DSC and are presented in Table 1. The pure BMI possesses the lowest  $T_g$  of  $\sim 210$  °C, close to the reported values [12]. Addition of graphite substantially improved the  $T_g$  by over 23%, with the BMI+25%Gr showing the highest  $T_g$  of 266°C, followed by those of BMI+40%Gr and BMI+55%Gr. The slightly lower  $T_g$  in the high graphite content composites indicate their decreased cross-linking degrees induced by presence of the graphite fillers, suggesting internal strength induced by cross-links tend to decline [12, 19, 39, 40].

**Table 1** Glass transition temperatures ( $T_g$ ) of BMI and BMI+Gr composites

Materials	BMI	BMI+25%Gr	BMI+40%Gr	BMI+55%Gr
$T_g$ (°C)	210	266	263	258

Mechanical properties of the BMI and BMI+Gr composites measured by nanoindentation are shown in Fig. 5, where hardness values and elastic moduli follow similar trend of rising rapidly with the graphite content increased from 0 to 25% yet keeping increasing slowly when continuously adding graphite. Apparently, graphite fillers here serve as not only solid lubricant but also reinforcement to improve mechanical property of the composites, leading to enhanced hardness and elastic modulus of 0.57 GPa and 8.3 GPa, respectively, at 55%Gr. Worth to note that BMI and BMI+Gr composites are relatively homogeneous (Fig. 5a insets) such that indentation results here represent the composites. The observed mechanical property is distinct from graphite-reinforced metal matrix composites (MMCs) and BMI-based nanocomposites. For MMCs, mechanical properties are often deteriorated with graphite content due to weak interface between metal and graphite [3, 6]. In BMI-based nanocomposites, there is an optimum solid lubricant content, often a few percent, beyond which mechanical properties declined [7, 8]. For instance, Fang *et al.* [41] fabricated BMI composites incorporating multiwall carbon nanotubes (MWCNTs), and they found that without surface treatment of nanotube, composites showed a hardness as low as the pure BMI, i.e.  $\sim 0.32$  GPa (HV $\sim 33$  in [41]). With nanotube functionalization, hardness was significantly improved to the maximum of 0.6 GPa (HV $\sim 65$  in [41]) with a content of  $\sim 2.5$  wt% and reduced rapidly to 0.54 GPa (HV $\sim 55$  in [41]) when the MWCNT content continued increasing. Such degradation of mechanical property originated from agglomeration of nanofillers at an increased content [7, 8]. Therefore, the consistently improved mechanical properties in the present work are likely associated with homogeneous distribution of the graphite particles as well as

interaction between polymer and graphite. Similar enhancement was also found in polystyrene/graphite composites [42]. Elastic moduli increased with graphite content up to 30 vol% and the improvement was more pronounced when graphite particle size was smaller. They attributed that to higher specific surface and thus more interaction between polymer and graphite [42].

## **3.2 Tribological behavior of the top polymer composites**

### **3.2.1 Friction and wear**

Fig. 6a presents coefficients of friction of the BMI and BMI+Gr composites versus cycle numbers, which exhibit a short running-in followed by a stable-state. Variation of the average friction taken from steady-state with graphite content is plotted in Fig. 6b; it reduces from  $\sim 0.58$  for pure BMI to the lowest value of  $\sim 0.15$  when the graphite content is 25%, then boosts slightly to 0.21 with further addition of graphite to 55%. Apparently, when the graphite content in the composites reaches and exceeds 25 wt% (i.e.  $\sim 17$  vol%), the friction coefficients keep relatively constant at a value of 0.15-0.21 and are virtually independent of graphite content. Given that a self-mated contact of graphite yields the lowest friction of  $\sim 0.18$  [43], it is reasonable to believe that in the present study, the contact including the steel counterfaces and wear tracks have been smeared with graphite.

Wear rates of the composites, shown in Fig. 6, decrease with graphite content from  $\sim 8 \times 10^{-6}$  mm<sup>3</sup>/Nm for neat BMI to  $\sim 0.4 \times 10^{-6}$  mm<sup>3</sup>/Nm at 55% graphite. The high standard deviation of the wear rate obtained in the BMI+55%Gr is likely induced by measurement difficulty because of very low wear rate. Clearly, wear rate of the composites consistently decreases with graphite content in a wide range of 0-55 wt%. This is distinct from self-lubricating metal matrix composites and BMI nanocomposites [3, 5-8, 41, 44]. In the latter, an optimum solid lubricant content often exists, beyond which wear rate increases [6-8, 41]. For example, BMI + nanographene + MoSe<sub>2</sub> hybrid composite yielded the lowest wear rate of  $\sim 2 \times 10^{-6}$  mm<sup>3</sup>/Nm when the reinforcement content was 0.4% [7]. This phenomenon was induced by degradation in mechanical properties [5-7]. Consequently, the present BMI+Gr composites distinguish themselves by the consistent improvement in wear resistance and mechanical properties with graphite content up to 55 wt%.

### 3.2.2 Transfer film formation

Generation and stability of transfer films on the counterface are considered as a key to maintain low friction and wear of a polymer composite [45-48]. It is associated with material transfer, adhesion of transfer film to the counterface, as well as morphology, chemical and mechanical properties of transfer films [45, 46, 48]. Here, transfer film characteristics during steady state were examined by optical microscopy and Raman spectroscopy. From Fig. 7a, the contact area sliding against BMI is not covered by transfer film with any detectable thickness after 3000 cycles. Instead, the softer polymer is scratched by the hard metal asperities and polymer fragments are deposited into the troughs, leaving traces of polymeric materials parallel to the sliding direction. Since this process could accumulate materials and generate transfer film on the counterface, the absence of transfer film demonstrates poor adhesion between BMI fragments and the steel counterface. The counterfaces against BMI+Gr composites shown in Fig. 7b-d, however, exhibit higher capacity of forming and maintaining transfer films during sliding. No significant trace marks of polymer but patchy transfer films are located at the center and the periphery of the contact. On the counterface against BMI+25%, the patchy transfer film comprises small pieces of transferred composite at the contact; yet large patches of transfer material are present at some areas of the contact periphery. The transfer material deposited at the contact periphery could serve as source to replenish formation of lubricating transfer film at the contact. With increase in graphite content, a greater amount of materials is deposited and attached onto the counterface in a more compacted manner, resulting in a highest transfer film coverage of ~17% at the BMI+55%Gr contact. Meanwhile, peripheries of the contacts are fully covered by a thin layer of transfer materials.

The above transfer film formation with graphite content indicates that the addition of graphite substantially improves the development of stable transfer films on the counterfaces, which demonstrates adhesion of the transfer materials and steel counterface is significantly enhanced. Then, the more complete transfer films protect the polymer composites from being scratched by the hard metal asperities, leading to low wear rates. Such effects of fillers on transfer film formation and wear have been found in various polymer composites. Bahadur and Tabor [49] observed a coherent transfer film was established when graphite or CuS filler was added to polytetrafluoroethylene (PTFE), which reduced the wear rate by a factor of 80-100 comparing to

that unreinforced PTFE. For an epoxy composite filled with graphite or PTFE, both fillers made contributions to development of more complete and coherent transfer films, hence significantly reduced wear rate from  $4 \times 10^{-6} \text{ mm}^3/\text{Nm}$  to  $0.6\text{-}0.9 \times 10^{-6} \text{ mm}^3/\text{Nm}$  [46]. A BMI+graphene/graphene-like  $\text{MoSe}_2$  nanocomposite produced the lowest wear rate at 0.4% fillers because a most coherent transfer film was formed at the contact [7]. Strong correlation between transfer film development and wear resistance in polymers and polymer composites was recently summarized by Ye *et al.* [48].

In Fig. 7e, Raman spectroscopy taken on the patchy transfer films and uncovered areas show strong characteristic graphite bands from the former and weak bands from the latter. This indicates no chemical reaction or phase transformation taken place in the sliding contact. More importantly, although there is no visible transfer film on the uncovered areas, a thin graphite-rich film is likely formed and separates direct contact of the steel counterface and the composites. Therefore, for the composites, sliding actually occurs between graphite-rich transfer films and wear tracks. This explains the friction evolution presented in Fig. 6, where it reduces to  $\sim 0.15$  at 25%Gr and keeps relatively constant at 0.15-0.21 with further increase in graphite content, and 25 wt% Gr (i.e.  $\sim 17 \text{ vol\%}$ ) is sufficient to minimize the friction to the level of self-mated contact of graphite [43].

### **3.3 Tribological behavior of the polymer-infiltrated-metal-network composites**

Before introducing tribological performances of the infiltrated metal-networks, morphology of the polished surfaces is presented. Taking the BMI+25%Gr specimen as an example, Fig. 8 shows plan view of the polished surface, from which area fraction of pores is measured as  $\sim 0.36\%$ , much lower than that observed from cross-sectional micrographs (i.e.  $\sim 3\text{-}5\%$ ). This demonstrates a higher tendency of forming pores with infiltration depth. The area fraction of the polymer composites is  $\sim 50\%$ . From Fig. 8b, the submicron graphite flakes are homogeneously distributed inside the BMI; yet several areas with  $1\text{-}2 \mu\text{m}$  in size may appear graphite rich. Surface topography in Fig. 8c reveals that the metal-network is higher than the polymer composite by  $1\text{-}3 \mu\text{m}$ , which is most likely due to lower material removal rate of the SS316L than that of polymers during polishing. This feature is commonly observed in the present work. For that reason, it is difficult to identify the unworn surface to precisely measure wear volume and to calculate wear rate as what

was done for the polymeric composites. Hence, only friction behaviour is presented here, followed by their capacity of developing lubricating transfer films and tribofilms.

### **3.3.1 Friction behaviour of the polymer-infiltrated-metal-network composites**

In order to reveal typical features of friction behaviour throughout sliding, friction evolution versus cycle numbers of the network infiltrated with BMI+25%Gr is shown in Fig. 9a, where it shows distinct characteristics from the top polymer composite (see Fig. 6a). After a short running-in of ~200 cycles, it reaches the first steady-state friction of 0.18-0.19 until ~4000 cycles, after which the friction starts climbing for roughly 2000 cycles, and eventually enters the second steady state, where the friction fluctuates between 0.24 and 0.26. Accordingly, four phases are assigned to express friction behaviour. As indicated in Fig. 9a, phase #1 refers to 200-2000 cycles, phase #2 2000-4000 cycles, phase #3 4000-6000 cycles, phase #4 6000-8000 cycles. Apparently, phase #1 exhibits more scattered friction coefficient than that of phase #2 regardless of both being in the first steady state. That is mainly induced by difference in wear track length; during phase #1, friction of each cycle is an average of friction values acquired along a 20-mm (200-1000 cycles) and later a 15-mm (1000-2000 cycles) wear track, that is shortened to 10 mm in phase #2. Therefore, phase #1 depicts spiky friction of the first steady state, and phase #2 illustrates less scattered portion of the first steady state. Phase #3 (5-mm wear track) indicates friction ascending to transition to the second steady state, and phase #4 (5-mm wear track) represents the second steady state.

Following the same procedure, four friction phases throughout each test of the four infiltrated composites are identified and their average values are plotted in Fig. 9b. The network filled with pure BMI shows the highest coefficients of friction at all phases, around 0.4-0.5 in the first steady state and ~0.57 in the second steady state. Their large standard deviations during two steady states indicate friction coefficients are spiky. Nevertheless, the networks infiltrated with polymer composites permit appreciably reduced friction, with the composite containing BMI+25%Gr ranging 0.18-0.26, BMI+40%Gr 0.25-0.28, and BMI+55%Gr 0.14-0.20. Unlike in the top polymer composites, where lowest friction is achieved at 25%Gr, the infiltrated networks exhibit minimum friction at 55%Gr. This could be interpreted by formation and replenishment of lubricating transfer films, which will be presented in detail in Section 3.3.2.

BMI- and BMI+25%Gr-infiltrated networks are featured by phase #3 of friction climbing, which becomes less noticeable with increase in graphite content to 40% and 55%. The number of cycles of phase #3 is shown in Fig. 9c, in which ~2250 cycles are required for the BMI+25%Gr-infiltrated network to transfer to the second steady state, and ~400 cycles for the BMI+40%Gr-infiltrated network, ~0 cycles when 55% graphite is added to the polymer. Therefore, friction of the BMI+55%Gr-infiltrated network displays one steady state throughout the test. But for graph plotting, selected cycle numbers of its each phase in Fig. 9b are the same as those in the BMI+25%Gr specimen.

### **3.3.2 Formation of lubricating transfer films and tribofilms at sliding contact**

As the BMI+25%Gr-infiltrated composite exhibits all typical features regarding tribological responses of the infiltrated metal-networks (see Fig. 9a), in this section, generation of lubricating tribofilms and transfer films at its contact during sliding is presented, based on which tribological performances of the other infiltrated composites may be understood.

Giving that metals and polymers have distinct mechanical properties, deformation of those two materials under sliding condition was investigated. Surface topography taken inside the wear tracks at 1000, 2000, 4000 and 8000 cycles and their corresponding optical micrographs are shown in Fig. 10. From Fig. 10a and 10e, at 1000 cycles, the metal parts in the middle of the wear track fall below the worn surface by 0.5-2  $\mu\text{m}$ , which is opposite to unworn surface, where the metal network stands out for 1-3  $\mu\text{m}$ . This drastic change could be driven by two reasons. First, the polymers often possesses significantly higher recovery or healing after deformation due to their viscoelasticity [50, 51]. For instance, scratch recovery of an epoxy at 70°C under various loads was as high as 65%, and it reached up to 95% by addition of a fluorinated poly(aryl ether ketone) (12F-PEK) [50]. Therefore, the polymeric phase may become higher than the metal network once sliding commences, and the real contact is then between the polymer composite and steel counterface. The second reason for the metal network sinking inside the wear track could be its low compressive strength. This contact scenario continues up to 2000 cycles, where the height difference is less than 1  $\mu\text{m}$  (see Fig. 10b and 10f). At 4000 cycles, the beginning of the friction transition stage, the metal becomes slightly higher than the polymer composite (see Fig. 10c and 10g). This indicates the contact condition has changed and the metallic phase in the composite

starts getting involved. At 8000 cycles, the second steady state, more polymer smears onto the metal surface, leaving no sharp interface between them, and the two phases share the same height (see Fig. 10d and 10h). Such observations on wear track topography are critical and provide essential information for further exploration on development of tribofilm and transfer film.

Material transfer and solid lubricant spreading at the contact during sliding are evaluated by optical microscopy and Raman spectroscopy. As shown in Fig. 11a, the two edges of the wear track at 1000 cycles are wavy, with metals standing out, which is caused by their greater height in the initial state. Sliding marks parallel to the sliding direction are likely induced by hard asperities on the counterface. From Fig. 11b-c, there are incomplete dark films smeared on the surface of the metal. The dark (point 1) and gray (point 2) films, examined by Raman spectroscopy, are rich in graphite and the higher intensity of signals in the dark film suggests the dark lubricating film is probably thicker. There are also bright spots (point 3) that are poor in graphite. Outside the metal, graphite-rich tribofilms are identified by the Raman spectroscopy (point 4). Small metallic particles are found well mixed with the polymer. Those particles may be produced at the onset of sliding where the real contact is between the steel counterface and metal network. While sliding continues to 2000 cycles, the above features in the wear track are maintained, as indicated in Fig. 11d-f. Since the metal network is lower in the wear tracks, material transfer is from the polymer composite to the metal surface. Meanwhile, lubricating films at the contact are formed easily and the transfer film on the counterface tend to be stable without interference of hard metals. This explains the low friction in the first steady states (see Fig. 9a-b).

In Fig. 12a-c, at 4000 cycles, beginning of the transition state, the metal surface has been largely covered by a layer that is rich in graphite (point 1). Well-developed lubricating tribofilms are formed inside the wear track except for some spots where metallic surface is exposed without a graphite-rich layer (point 2). As metals are slightly higher in the wear track at this point (see Fig. 10c), some lubricating transfer film will be easily removed with sliding continues, resulting in increase in friction (see Fig. 9a). As shown in Fig. 12d-f, during the second steady state (at 8000 cycles), the polymeric phase is transferred to metal surface to a greater extent, evidenced by the wear track that is almost fully covered by polymeric materials that is graphite rich.

Because formation of transfer film becomes more complicated when the metallic phase in the composites gets involved, transfer film characteristics at 4000 and 8000 cycles were examined more carefully. From Fig. 13a-c, at 4000 cycles, the contact area on the counterface is fully covered by a thin transfer film, with loose wear debris accumulated at the edge. Raman analysis on those features show they are rich in graphite. Flattened topography of the counterface exhibits no detectable height difference between the contact and unworn area, indicating no counterface wear taken place by the end of the first steady state. However, because some metallic phase is slightly higher than the polymer in the wear track, part of transfer film could be removed when sliding continuously. That is confirmed by the patchy transfer film observed at 8000 cycles, as seen in Fig. 13d-f, where only a small patch of transfer film remains. It appears powdery and contains graphite. From flattened topography of the counterface, the areas uncovered by transfer film is lower than the unworn reference by roughly  $4\text{ }\mu\text{m}$ , demonstrating the counterface has been severely worn during the second steady state. With most of the contact being metal, relatively high friction coefficient is yielded from the BMI+25%Gr-infiltrated composite (see Fig. 9a). Therefore, a key to reduce friction and eliminate the friction transition and second steady state is to improve transfer film formation and establish fully lubricating contact.

Accordingly, one may expect the low friction of  $\sim 0.2$  for the BMI+55%Gr-infiltrated network is likely driven by sufficient replenishment to the lubricating transfer film because of its higher capacity of transfer film formation (see Fig. 7). Indeed, the volume fraction of graphite in the infiltrated composite is  $\sim 22\%$  that has reached the critical value, i.e.  $\sim 20\%$ , experimentally observed in graphite-reinforced metal matrix composites, to form fully lubricating transfer films [6, 43]. Therefore, no transition phase observed in the BMI+55%Gr-infiltrated network, and it becomes longer with decrease in graphite (Fig. 9c). For the BMI+40%Gr-infiltrated network, except for uncomplete transfer film, the higher friction than that of BMI+25%Gr-infiltrated composite is likely due to reduced  $T_g$  of the polymer, as explained previously.

Given that in the present work, the top polymer composites were removed artificially by polishing, the gradual transition from the top layer to the infiltrated metal-network that will occur when this material is put into applications is missing. A reasonable prediction is that with the top polymer composites, the first steady state of the infiltrated composites may last longer due to pre-existing transfer film, yet the other features may remain. The second interesting open question is how



mechanical properties of the metal network affect material transfer and transfer film formation. Third, due to distinct thermal expansion coefficients between polymer and metal, residual stress is likely produced during curing and cooling. Whether and how it influences tribological performance are still unknown.

## 4 Conclusions

In summary, self-lubricating duplex composites including a top layer of polymer-based composite reinforced with graphite and a bottom layer of infiltrated metal-network were manufactured by a hot compression-molded method. According to the manufacturing process, mechanical properties and tribological performances of the duplex composites, the following conclusions can be drawn:

- The BMI possesses a strong capacity of loading graphite fillers (up to 55 wt%), which is due to its good flowability and wide processing window. The infiltration depth reduces with increasing graphite content, from  $\sim 1600\ \mu\text{m}$  for BMI to  $\sim 185\ \mu\text{m}$  for BMI+55%Gr.
- The glass transition temperature of the composites decreases with graphite content, which is due to less cross-linking sites available because of the graphite fillers. But the elastic modulus and hardness of the composites increase with graphite content without degradation, reaching the highest hardness of 0.57 GPa at 55wt% loading of graphite.
- For the top polymer-based composites, 25 wt% graphite is sufficient to reduce friction to the lowest value of  $\sim 0.15$  because of the formation of lubricating transfer film. The wear rate decreases consistently with graphite content, which is driven by improved mechanical property and capacity to form stable transferfilms.
- For the bottom infiltrated composites, friction evolution with cycle numbers typically includes a first steady-state of low friction, transition stage, and a second steady-state of high friction. The first steady state relates to formation of fully covered graphite-rich transfer film and tribofilm; transition stage starts once metallic phase gets into the contact and transfer film cannot be replenished, leading to friction ascending; during the second steady state, most of the contact is not covered by transfer film, leading to high friction and counterface wear. However, the BMI+55%Gr-infiltrated network that contains  $\sim 22\ \text{vol}\%$  graphite effectively replenishes transfer film and eliminates transition phase.

- The current work demonstrates such duplex composites can be successfully manufactured and future perspective is possible engineering applications to components in forms of metallic foams or 3-D printed structures or porous coatings.

## Acknowledgements

The authors gratefully acknowledge the financial support from Natural Sciences and Engineering Research Council (NSERC) of Canada. They gratefully acknowledge Mr. Sylvio Savoie (IREQ) for technical assistance on polymer infiltration process, Sodelwyn Yit (McGill University) for sample preparation.

## References

1. Carpick, R.W., A. Jackson, W.G. Sawyer, N. Argibay, P. Lee, A. Pachon, and R.M. Gresham, *The tribology opportunities study: can tribology save a quad?* Tribology & Lubrication Technology, 2016. **72**(5): p. 44.
2. Holmberg, K. and A. Erdemir, *The impact of tribology on energy use and CO2 emission globally and in combustion engine and electric cars.* Tribology International, 2019. **135**: p. 389-396.
3. Omrani, E., A.D. Moghadam, P.L. Menezes, and P.K. Rohatgi, *Influences of graphite reinforcement on the tribological properties of self-lubricating aluminum matrix composites for green tribology, sustainability, and energy efficiency—a review.* The International Journal of Advanced Manufacturing Technology, 2016. **83**(1-4): p. 325-346.
4. Zhang, Y., J.M. Shockley, P. Vo, and R.R. Chromik, *Tribological Behavior of a Cold-Sprayed Cu–MoS2 Composite Coating During Dry Sliding Wear.* Tribology Letters, 2016. **62**(1): p. 1-12.
5. Moghadam, A.D., E. Omrani, P.L. Menezes, and P.K. Rohatgi, *Mechanical and tribological properties of self-lubricating metal matrix nanocomposites reinforced by carbon nanotubes (CNTs) and graphene—a review.* Composites Part B: Engineering, 2015. **77**: p. 402-420.
6. Zhang, Y. and R.R. Chromik, *Tribology of Self-Lubricating Metal Matrix Composites*, in *Self-Lubricating Composites*. 2018, Springer. p. 33-73.
7. Chen, Z., L. Guo, H. Yan, H. Yao, L. Li, and Q. Liu, *Amino functionalization of graphene/graphene-like MoSe2 hybrids as lubricant additives for bismaleimide composites: Preparation, mechanical and tribological properties.* Composites Part B: Engineering, 2019. **161**: p. 263-271.
8. Chen, Z., H. Yan, T. Liu, and S. Niu, *Nanosheets of MoS2 and reduced graphene oxide as hybrid fillers improved the mechanical and tribological properties of bismaleimide composites.* Composites Science and Technology, 2016. **125**: p. 47-54.
9. Torres, H., M. Rodríguez Ripoll, and B. Prakash, *Tribological behaviour of self-lubricating materials at high temperatures.* International Materials Reviews, 2018. **63**(5): p. 309-340.
10. Brostow, W., E.H.H. Lobland, N. Hnatchuk, and M.J. Perez, *Improvement of Scratch and Wear Resistance of Polymers by Fillers Including Nanofillers.* Nanomaterials, 2017. **7**(3).

11. Thunga, M., K. Larson, W. Lio, T. Weerasekera, M. Akinc, and M.R. Kessler, *Low viscosity cyanate ester resin for the injection repair of hole-edge delaminations in bismaleimide/carbon fiber composites*. Composites Part A: Applied Science and Manufacturing, 2013. **52**: p. 31-37.
12. Campbell, F.C., *Chapter 3 - Thermoset Resins: The Glue That Holds the Strings Together*, in *Manufacturing Processes for Advanced Composites*, F.C. Campbell, Editor. 2004, Elsevier Science: Amsterdam. p. 63-101.
13. Sava, M., *Syntheses of bismaleimides with ester units and their polymerization with diamines*. Journal of applied polymer science, 2002. **84**(4): p. 750-757.
14. Tewari, U., S. Sharma, and P. Vasudevan, *Friction and wear studies of a bismaleimide*. Tribology international, 1988. **21**(1): p. 27-30.
15. Wang, G., D. Yu, A.D. Kelkar, and L. Zhang, *Electrospun nanofiber: Emerging reinforcing filler in polymer matrix composite materials*. Progress in Polymer Science, 2017. **75**: p. 73-107.
16. Bhargava, S., M.E. Makowiec, and T.A. Blanchet, *Wear reduction mechanisms within highly wear-resistant graphene- and other carbon-filled PTFE nanocomposites*. Wear, 2020. **444-445**: p. 203163.
17. Makowiec, M.E. and T.A. Blanchet, *Improved wear resistance of nanotube-and other carbon-filled PTFE composites*. Wear, 2017. **374**: p. 77-85.
18. YanáMa, X., *Hyperbranched polysiloxane grafted graphene for improved tribological performance of bismaleimide composites*. RSC Advances, 2015. **5**(17): p. 12578-12582.
19. Liu, L., A. Gu, Z. Fang, L. Tong, and Z. Xu, *The effects of the variations of carbon nanotubes on the micro-tribological behavior of carbon nanotubes/bismaleimide nanocomposite*. Composites Part A: Applied Science and Manufacturing, 2007. **38**(9): p. 1957-1964.
20. Nascimento, A.R., S. Devaraj, A.P. Francelin, S. Savoie, R. Schulz, and C. Moreau, *Tailored Porosity for Polymer Infiltration in Stainless Steel Coatings*. Journal of Thermal Spray Technology, 2019. **28**(6): p. 1173-1184.
21. Ojha, N. and N. Das, *A statistical approach to optimize the production of polyhydroxyalkanoates from Wickerhamomyces anomalus VIT-NN01 using response surface methodology*. International journal of biological macromolecules, 2018. **107**: p. 2157-2170.
22. Brostow, W., V. González, J.M. Perez, and S.C. Shipley, *Wetting angles of molten polymers on thermoelectric solid metal surfaces*. Journal of Adhesion Science and Technology, 2019: p. 1-9.
23. Eustathopoulos, N., N. Sobczak, A. Passerone, and K. Nogi, *Measurement of contact angle and work of adhesion at high temperature*. Journal of Materials Science, 2005. **40**(9-10): p. 2271-2280.
24. Kaplan, W.D., D. Chatain, P. Wynblatt, and W.C. Carter, *A review of wetting versus adsorption, complexions, and related phenomena: the rosetta stone of wetting*. Journal of Materials Science, 2013. **48**(17): p. 5681-5717.
25. Rahmat, M. and P. Hubert, *Carbon nanotube–polymer interactions in nanocomposites: a review*. Composites Science and Technology, 2011. **72**(1): p. 72-84.
26. Guseva, O., H.R. Lusti, and A.A. Gusev, *Matching thermal expansion of mica–polymer nanocomposites and metals*. Modelling and Simulation in Materials Science and Engineering, 2004. **12**(3): p. S101.

27. Beake, B.D. and J.F. Smith, *High-temperature nanoindentation testing of fused silica and other materials*. Philosophical Magazine A, 2002. **82**(10): p. 2179-2186.
28. Oliver, W.C. and G.M. Pharr, *An improved technique for determining hardness and elastic modulus using load and displacement sensing indentation experiments*. Journal of materials research, 1992. **7**(06): p. 1564-1583.
29. Chromik, R., H. Strauss, and T. Scharf, *Materials phenomena revealed by in situ tribometry*. JOM, 2012. **64**(1): p. 35-43.
30. Lee, L., P. Behera, K.R. Sriraman, and R.R. Chromik, *Effects of humidity on the sliding wear properties of Zn–Ni alloy coatings*. RSC Advances, 2017. **7**(37): p. 22662-22671.
31. Wahl, K.J., D.N. Dunn, and I.L. Singer, *Wear behavior of Pb–Mo–S solid lubricating coatings*. Wear, 1999. **230**(2): p. 175-183.
32. Nicodemo, L. and L. Nicolais, *Mechanical properties of metal/polymer composites*. Journal of Materials Science Letters, 1983. **2**(5): p. 201-203.
33. Greenwood, P., R. Thring, and R. Chen, *Material property models for polyethylene-based conductive blends suitable for PEM fuel cell bipolar plates*. Proceedings of the Institution of Mechanical Engineers, Part L: Journal of Materials: Design and Applications, 2016. **230**(1): p. 131-141.
34. Miyamoto, Y., W.A. Kaysser, B.H. Rabin, A. Kawasaki, and R.G. Ford, *Modeling and Design*, in *Functionally Graded Materials: Design, Processing and Applications*, Y. Miyamoto, et al., Editors. 1999, Springer US: Boston, MA. p. 63-88.
35. Seo, M.-K. and S.-J. Park, *Electrical resistivity and rheological behaviors of carbon nanotubes-filled polypropylene composites*. Chemical Physics Letters, 2004. **395**(1-3): p. 44-48.
36. King, J.A., F.A. Morrison, J.M. Keith, M.G. Miller, R.C. Smith, M. Cruz, A.M. Neuhalfen, and R.L. Barton, *Electrical conductivity and rheology of carbon - filled liquid crystal polymer composites*. Journal of applied polymer science, 2006. **101**(4): p. 2680-2688.
37. Lin, T., S. Wu, J. Lai, and S. Shyu, *The effect of chemical treatment on reinforcement/matrix interaction in Kevlar-fiber/bismaleimide composites*. Composites Science and Technology, 2000. **60**(9): p. 1873-1878.
38. Su, M., A. Gu, G. Liang, and L. Yuan, *The effect of oxygen-plasma treatment on Kevlar fibers and the properties of Kevlar fibers/bismaleimide composites*. Applied Surface Science, 2011. **257**(8): p. 3158-3167.
39. Campbell, F.C., *Chapter 6 - Curing: It's a Matter of Time (t), Temperature (T) and Pressure (P)*, in *Manufacturing Processes for Advanced Composites*, F.C. Campbell, Editor. 2004, Elsevier Science: Amsterdam. p. 175-221.
40. Campbell Jr, F.C., *Manufacturing processes for advanced composites*. 2003: elsevier.
41. Fang, Z., L. Liu, A. Gu, X. Wang, and Z. Guo, *Improved microhardness and microtribological properties of bismaleimide nanocomposites obtained by enhancing interfacial interaction through carbon nanotube functionalization*. Polymers for Advanced Technologies, 2009. **20**(11): p. 849-856.
42. Krupa, I. and I. Chodák, *Physical properties of thermoplastic/graphite composites*. European Polymer Journal, 2001. **37**(11): p. 2159-2168.
43. Rohatgi, P.K., S. Ray, and Y. Liu, *Tribological properties of metal matrix-graphite particle composites*. International Materials Reviews, 1992.

44. Omrani, E., B. Barari, A.D. Moghadam, P.K. Rohatgi, and K.M. Pillai, *Mechanical and tribological properties of self-lubricating bio-based carbon-fabric epoxy composites made using liquid composite molding*. Tribology International, 2015. **92**: p. 222-232.
45. Bahadur, S., *The development of transfer layers and their role in polymer tribology*. Wear, 2000. **245**(1-2): p. 92-99.
46. Chang, L., Z. Zhang, L. Ye, and K. Friedrich, *Tribological properties of epoxy nanocomposites: III. Characteristics of transfer films*. Wear, 2007. **262**(5): p. 699-706.
47. Ma, J., X. Qi, Y. Dong, Y. Zhao, Q. Zhang, B. Fan, and Y. Yang, *Transfer film formation mechanism and tribochemistry evolution of a low-wear polyimide/mesoporous silica nanocomposite in dry sliding against bearing steel*. Tribology International, 2018. **120**: p. 233-242.
48. Ye, J., D. Burris, and T. Xie, *A review of transfer films and their role in ultra-low-wear sliding of polymers*. Lubricants, 2016. **4**(1): p. 4.
49. Bahadur, S. and D. Tabor, *The wear of filled polytetrafluoroethylene*. Wear, 1984. **98**: p. 1-13.
50. Brostow, W., B. Bujard, P.E. Cassidy, H.E. Hagg, and P.E. Montemartini, *Effects of fluoropolymer addition to an epoxy on scratch depth and recovery*. Materials Research Innovations, 2002. **6**(1): p. 7-12.
51. Brostow, W., H.E. Hagg Lobland, and M. Narkis, *Sliding wear, viscoelasticity, and brittleness of polymers*. Journal of Materials Research, 2006. **21**(9): p. 2422-2428.

#### Figure captions:

**Fig. 1** (a) TGA measurement of the as-received polymer; (b) DSC measurement of the as-received polymer, inset is the contact angle measurement of the polymer at ~138 °C.

**Fig. 2** DSC thermograms of BMI and BMI+Gr mixes showing the melting peaks (a), polymerization peaks (b) at a heating rate of 10 °C/min.

**Fig. 3** (a) Processing parameters including temperature, pressure, and time of infiltration and curing. (b) and (c) are schematic drawings, respectively, of blend of polymer and graphite powders placed onto a metal network prior to the platens being closed, and the resultant duplex composite. Typical thickness of the metal network, the top polymer composite and infiltrated metal network are marked in (b) and (c).

**Fig. 4** (a) Infiltration depth versus graphite content; insets (a1) and (a2) exhibit cross-sectional optical micrographs of pure BMI and BMI+55% Gr. (b) Optical micrograph of the BMI infiltrated metal network. The black arrows indicate infiltration direction.

**Fig. 5** (a) Hardness and elastic modulus of the cured BMI and BMI+Gr composites versus graphite content measured by nanoindentation, insets a1 and a2 show typical optical micrographs of pure BMI and BMI+55%Gr composite, respectively; (b) Typical load-displacement curves of the cured BMI and BMI+Gr composites.

**Fig. 6** Coefficients of friction vs. cycle number (a) and average coefficients of friction and wear rates (b) of the top layers of BMI and BMI+Gr composites versus graphite content.

**Fig. 7** Optical micrographs of the counterfaces that slid against pure BMI (a), BMI+25%Gr (b), BMI+40%Gr (c), and BMI+55%Gr (d) after 3000 cycles; (e) characteristic Raman spectra of the transfer films and the uncovered area outside the patchy transfer films. The dashed lines in (a) indicate contact area, the left and right arrows indicate sliding direction.

**Fig. 8** (a) (b) Typical optical micrographs and (c) surface topography of the BMI+25%Gr-infiltrated metal-networks after polishing. The black arrows mark graphite-rich areas.

**Fig. 9** (a) Typical friction evolution with cycle number, in which four sections are identified; (b) A plot of average coefficients of friction of each section of the BMI and BMI+Gr composites; (c) Cycle numbers required for the transition section (i.e. stage 3) versus graphite contents of the composites.

**Fig. 10** Typical topography and corresponding optical micrographs of wear tracks at 1000 cycles (a & e), 2000 cycles (b & f), 4000 cycles (c & g), and 8000 cycles (d & h). The left and right arrows indicate sliding direction.

**Fig. 11** Optical micrographs of the wear track morphology at 1000 cycles (a & b), and 2000 cycles (d & e). (c) and (f) are Raman spectra from the spots indicated in (b) and (e), respectively. The black dashed lines in (a) and (d) highlight the wear track edges. The black arrows in (a) and (d) mark metals stand out. The left and right arrows indicate sliding direction.

**Fig. 12** (a) Optical micrographs of the wear track morphology at 4000 cycles (a & b), and 8000 cycles (d & e). (c) and (f) are Raman spectra from the spots noted in (b) and (e), respectively. The left and right arrows indicate sliding direction.

**Fig. 13** (a) Optical micrograph and flattened topography of the counterface at 4000 cycles (a & b), and 8000 cycles (d & e). (c) and (f) are Raman spectra from the features indicated in (a) and (d), respectively. The white dashed lines in (b) and (e) highlight the contact areas. The left and right arrows indicate sliding direction.

Fig. 1

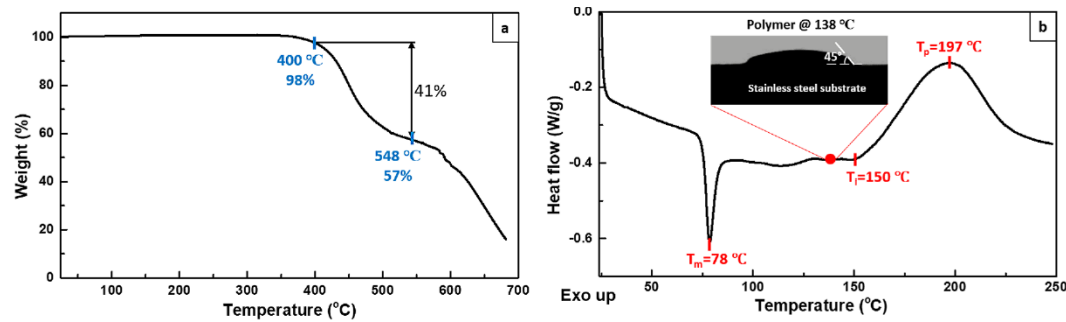


Fig. 2

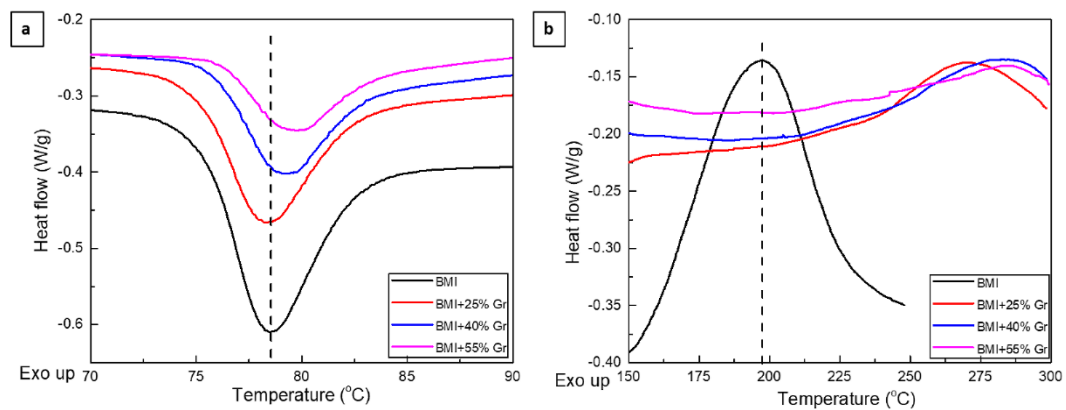


Fig. 3

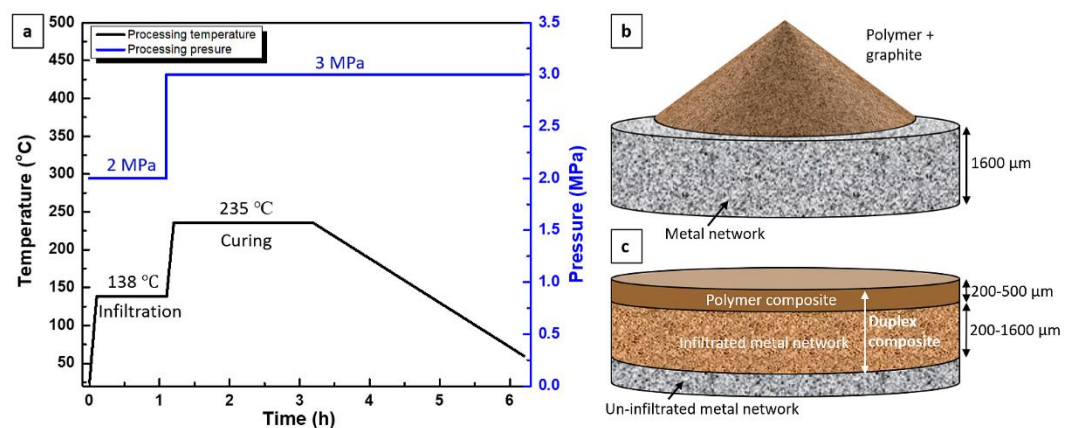


Fig. 4

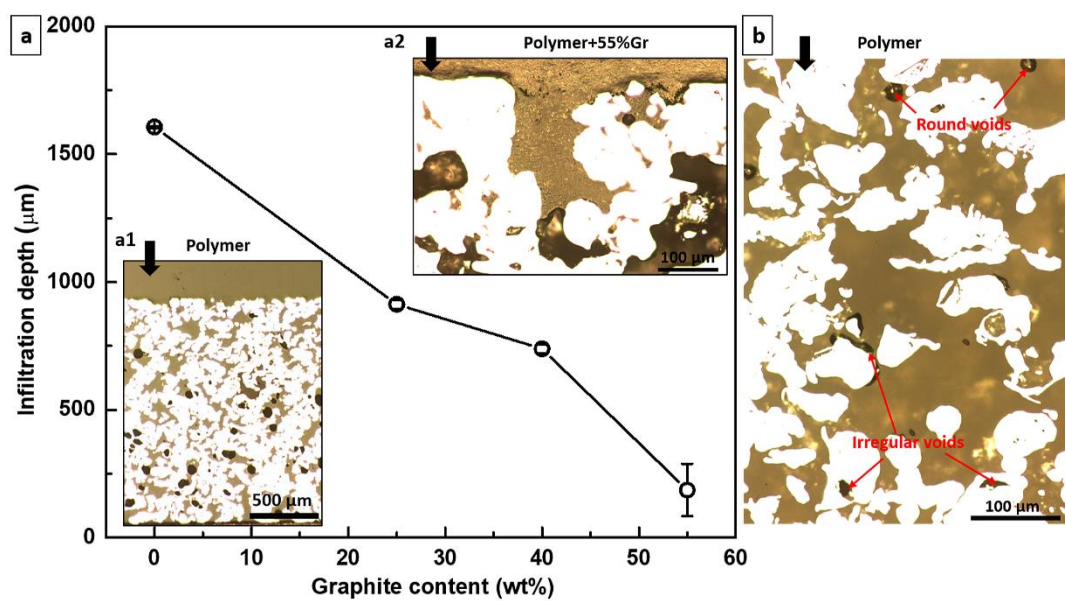




Fig. 5

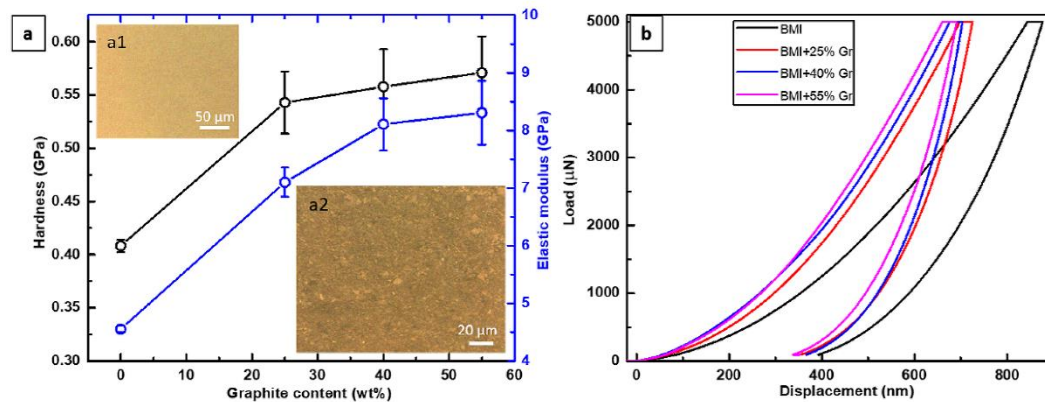


Fig. 6

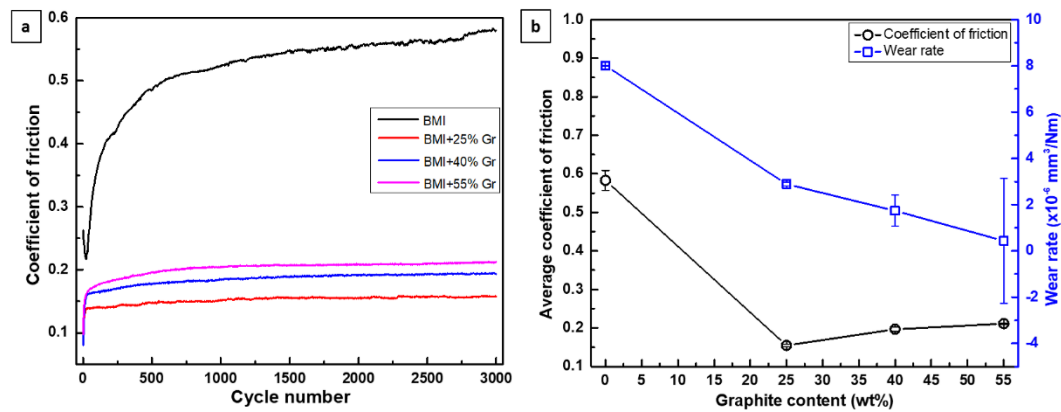


Fig. 7

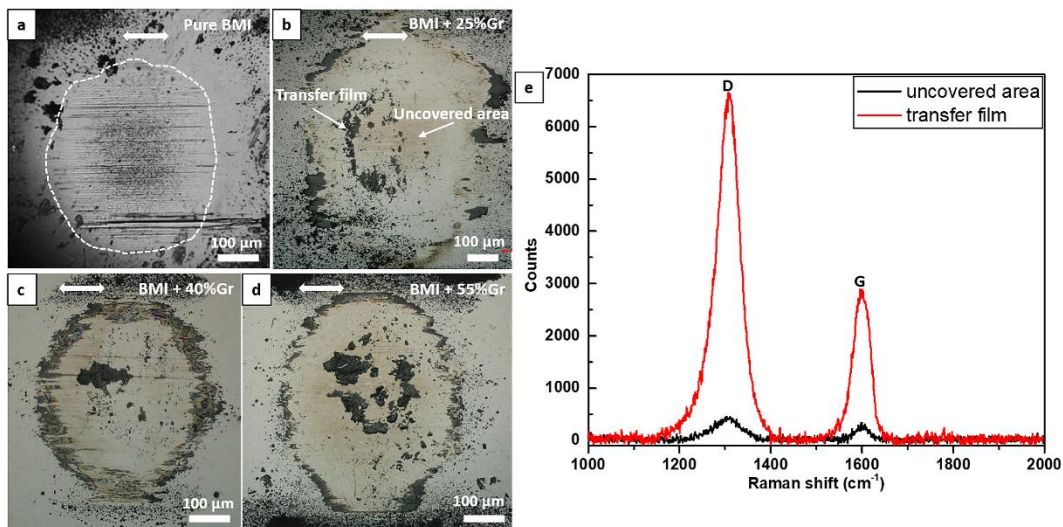




Fig. 8

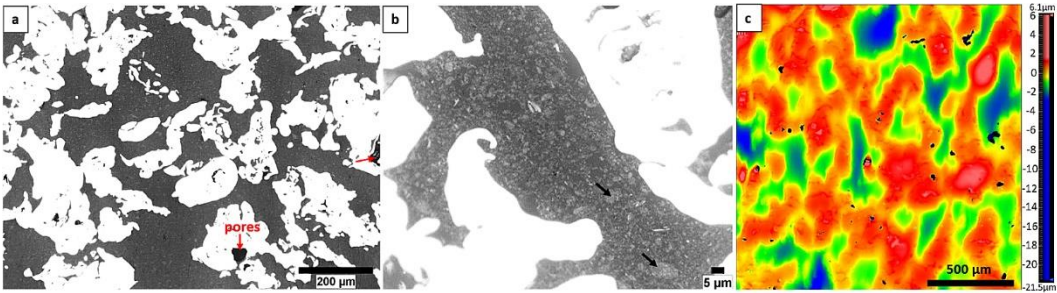


Fig. 9

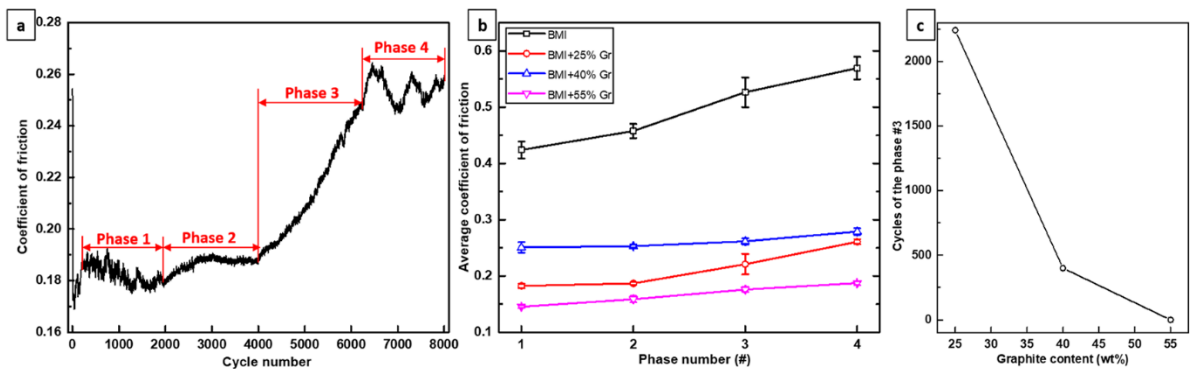


Fig. 10

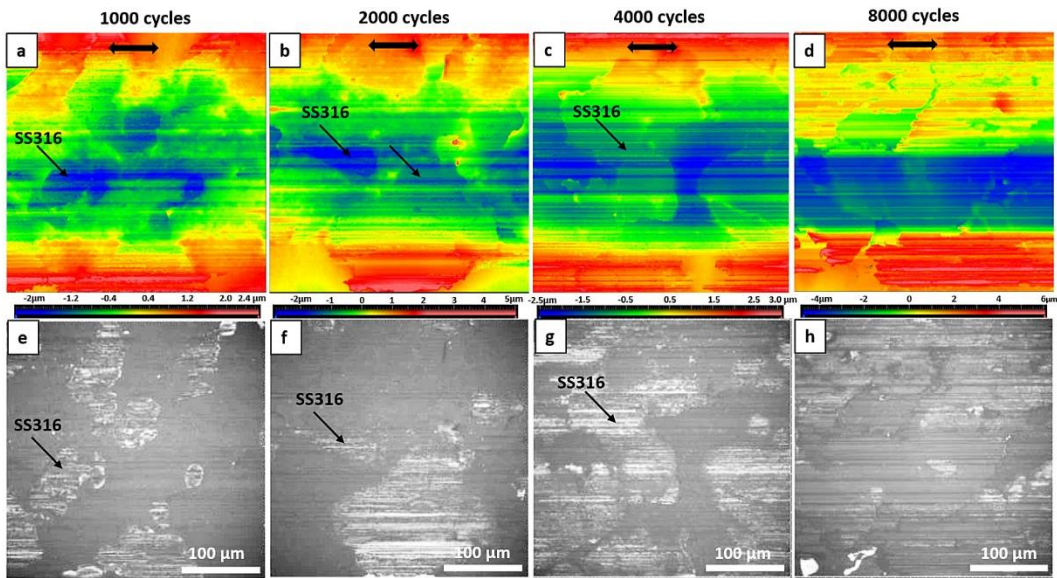


Fig. 11

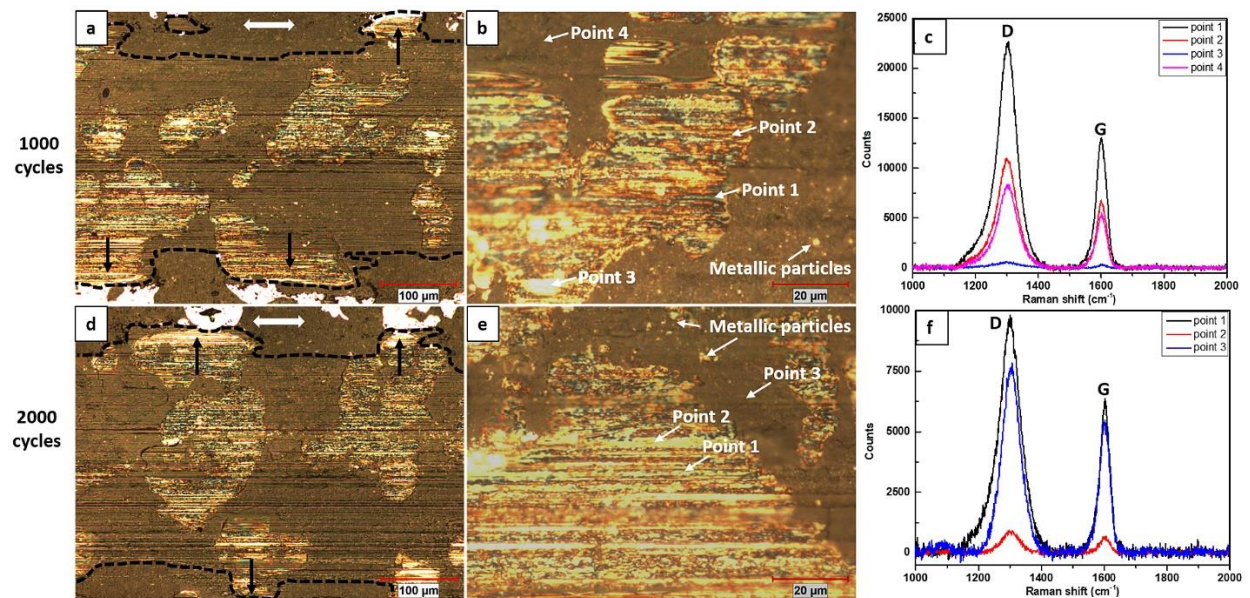


Fig. 12

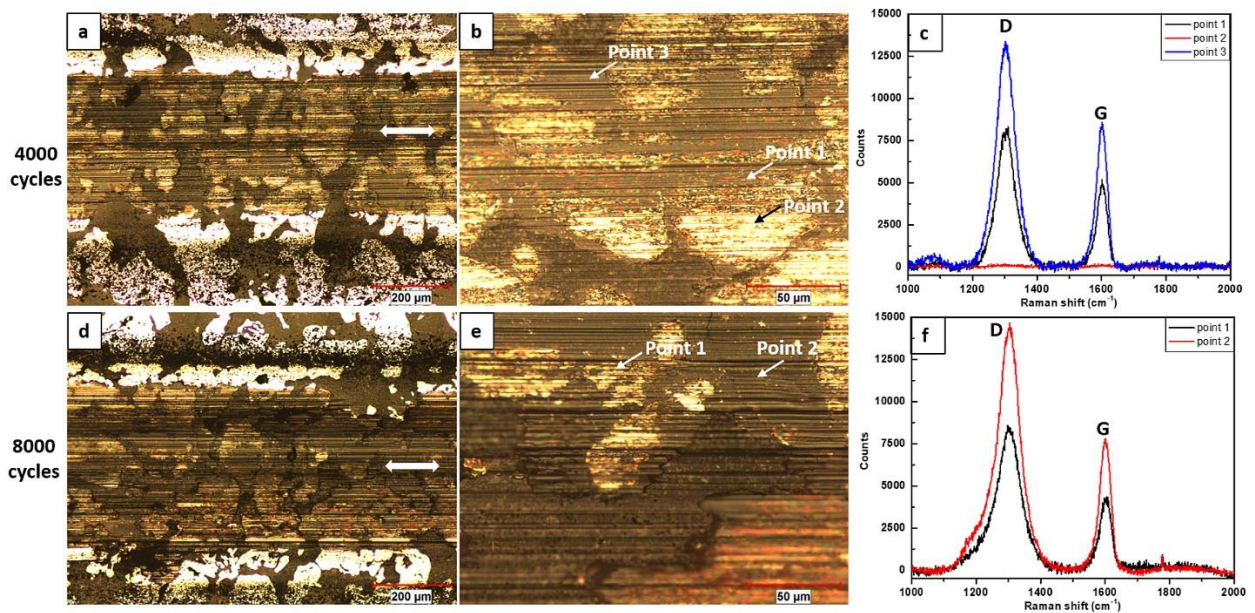




Fig. 13

